Exploring the RNA-Binding Potential of Three-Dimensional Cyanines Derived From [2.2]Paracyclophane: A Structure–Property Relationship

Rongyu Sun, Cristian Siretanu, Georgina Ilieska, Simon Felder, Erica Benedetti, Laurent Micouin

ChemBioChem

Chemistry Europe
European Chemical Societies Publishing
ChemBioChem

RESEARCH ARTICLE OPEN ACCESS

Exploring the RNA-Binding Potential of Three-Dimensional Cyanines Derived From [2.2]Paracyclophane: A Structure–Property Relationship

Rongyu Sun | Cristian Siretanu | Georgina Ilieska | Simon Felder | Erica Benedetti | Laurent Micouin

Laboratoire de Chimie et de Biochimie Pharmacologiques et Toxicologiques, Université Paris Cité, CNRS, Paris, France

Correspondence: Erica Benedetti (erica.benedetti@u-paris.fr) | Laurent Micouin (laurent.micouin@u-paris.fr)

Received: 31 October 2025 | **Revised:** 11 December 2025 | **Accepted:** 15 December 2025

Keywords: cyanines | 3D aromatic compounds | [2.2]Paracyclophanes | RNA binders | turn-on fluorescent dyes

ABSTRACT

This study reports the design, synthesis, and structure–property analysis of an original family of three-dimensional cyanine dyes based on the [2.2]paracyclophane (pCp) scaffold. By converting planar polymethine chromophores into three-dimensional architectures, we developed fluorogenic dyes with enhanced selectivity for single-stranded RNA containing stem-loop motifs. Comparative studies with planar analogs show that benzothiazole- and benzoselenazole-containing pCp derivatives exhibit strong fluorescence turn-on upon nucleic-acid binding, with responses varying by nucleic acid type and structure. Circular dichroism analyses suggest that these three-dimensional dyes interact with RNA via a nonintercalative mode, distinct from classical planar intercalators. Expanding upon preliminary findings, this work explores an extended series of pCp-derived cyanines, revealing how three-dimensionality modulates both photophysical behavior and nucleic-acid recognition. These results provide new directions for the design of selective RNA-targeting ligands and for future exploration of their interactions with more complex RNA architectures.

1 | Introduction

The central dogma of biology describes the flow of genetic information from DNA to RNA and, ultimately, to proteins, which are traditionally considered the primary functional macromolecules in cells [1, 2]. However, only 1.5% of the human transcriptome—the complete set of RNA molecules transcribed from the genome—codes for proteins [3, 4]. The vast majority of RNAs are noncoding and play essential roles in regulating a wide range of cellular processes. Noncoding RNAs are increasingly recognized for their critical involvement in the development of various diseases, including cancer, neurological disorders, and cardiovascular conditions [5].

Historically, drug development has predominantly focused on targeting proteins, but relying solely on this approach greatly limits our ability to effectively treat a wide range of diseases. As a result, RNA has recently emerged as a promising alternative target in medicinal chemistry, opening new possibilities for expanding therapeutic strategies and addressing previously untreatable conditions [6–8].

Two main approaches are currently being explored to modulate RNA functions: treating the biomolecule as a linear sequence of nucleotides or as a structured three-dimensional entity. The first approach has led to the development of antisense oligonucleotides (ASOs) [9, 10], some of which are already commercially available. However, this method often involves designing highly charged compounds with multiple hydrogen bond donor or acceptor motifs, which pose challenges in terms of synthesis, storage, administration, and in vivo delivery [11, 12]. In contrast, the second approach takes inspiration from protein targeting, focusing on recognizing specific structured regions of RNA using small molecules [13–15]. This strategy has recently shown considerable promise, as exemplified by the FDA's approval of

Risdiplam [16–18], a drug for treating spinal muscular atrophy. However, this orally bioavailable molecule was discovered through phenotypic screening rather than initial rational design, with its target and mechanism of action only identified after its effectiveness was demonstrated in clinical studies [19].

Despite significant progress in understanding the principles for rationally designing compounds with high affinity for relevant RNA targets [20, 21], clear guidelines for enhancing the selectivity of RNA/small molecule interactions remain elusive. This limitation continues to significantly hinder the full therapeutic potential of RNA-targeting small molecules. Advancing our understanding of how small molecules selectively interact with structured RNA motifs is crucial to develop more effective compounds, particularly when the RNA target is not overexpressed. Recent studies suggest that exploring chemical space beyond traditional "flat" aromatic molecules may present promising opportunities for developing more selective RNA ligands. Indeed, compounds such as spirocycles and triptycenes have been identified for their ability to target low-complexity RNA structural motifs, such as bulges and three-way junctions (Figure 1) [22–28]. Spirocycles and triptycenes feature rigid non-coplanar aromatic moieties that interact with the unpaired regions of RNA through π-stacking. Moreover, their three-dimensional shape reduces nonselective interactions, such as intercalation into duplex regions or groove binding, making them strong candidates for therapeutic development [29].

Building on these pioneering examples, we sought to improve the selectivity of previously described RNA ligands by introducing unconventional three-dimensional elements into their structures. In a preliminary investigation, we synthesized a cyanine derivative incorporating a [2.2]paracyclophane (pCp) scaffold, inspired by a previously reported "flat" molecule [30–32]. The pCp moiety is a bicyclic system with two fuzed benzene rings connected by ethylene bridges, creating a rigid, three-dimensional architecture with an inter-ring distance of ≈3.4 Å, sufficient to reduce intercalation into double-helical regions of DNA and RNA [33]. Incorporating the pCp motif into the cyanine core transformed the molecule from a planar to a three-dimensional shape, resulting in a fluorogenic ligand capable of differentiating among various nucleic acids, including DNA, rRNA, and tRNA. Interestingly, the three-dimensional dye exhibited preferential binding to single-stranded RNA sequences containing large stem-loop structures [34].

In contrast to our earlier, more limited proof of concept, the present work systematically expands this strategy by investigating a diverse set of cyanine dyes (Figure 1). This broader approach enables the establishment of detailed structure–property relationships, offering deeper insights into how three-dimensional modifications affect both the photophysical properties of the dyes and their RNA recognition capabilities. By doing so, the study opens new avenues for the rational design of selective RNA-targeting ligands, advancing beyond the initial proof-of-concept and laying the groundwork for the development of novel RNA binders and chemical probes.

2 | Results and Discussion

2.1 | Synthetic Procedures

We began our investigations by designing efficient synthetic pathways to prepare a series of *para*-disubstituted polymethines derived from pCp. All the desired compounds were prepared starting from a key aldehyde intermediate [35]. The synthesis of this intermediate, which features a dimethylamino moiety and a formyl group on the same aromatic ring of the pCp core, started with a nitration reaction carried out using nitric acid and sulfuric acid in dichloromethane. The resulting product was then reduced using Fe in HCl, affording compound **1** in a 51% yield. Next, a dimethylation under reductive amination conditions, followed by a *para*-selective Vilsmeier-Haack formylation, provided product **3** with an overall yield of 42% (Scheme 1).

To access the target compounds in a more straightforward manner, we revisited and optimized the synthesis of the pCp-based cyanine previously developed in our laboratory [34]. In our earlier work, the preparation of the desired dye required a two-step sequence involving a Wittig-type transformation, followed by methylation. In contrast, the same molecule containing

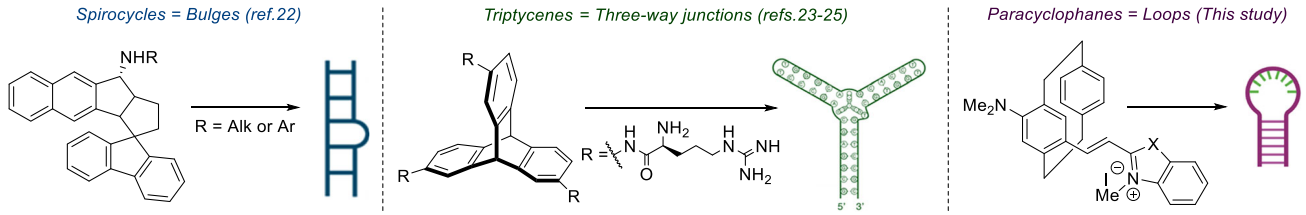

FIGURE 1 | 3D small molecules binding to RNA motifs of low complexity.

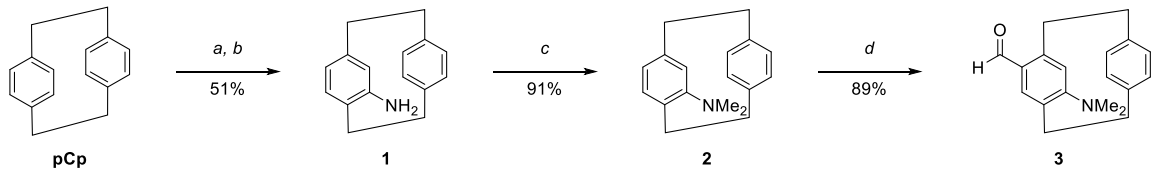

SCHEME 1 | Synthesis of key aldehyde intermediate **3**. Reaction conditions: (a) H_2SO_4 (4 equiv.), HNO_3 (2 equiv.), CH_2Cl_2, 0°C to rt, overnight; (b) Fe (12 equiv.), HCl, EtOH, H_2O, rt to 80°C, 2 h; (c) Paraformaldehyde (10 equiv.), $NaBH_3CN$ (5 equiv.), CH_3CO_2H, 0°C to rt, 16 h; (d) $POCl_3$ (1 equiv.), DMF, 0°C to 100°C, 3 h.

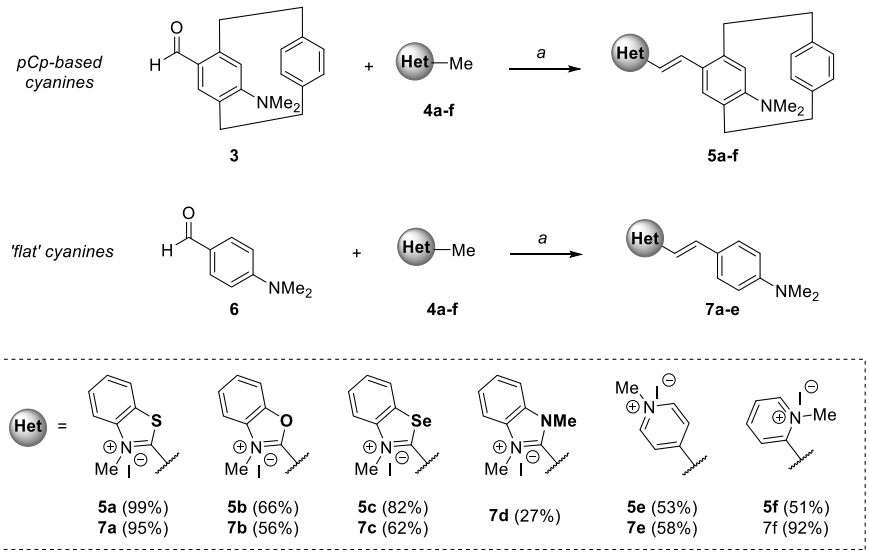

SCHEME 2 | Knoevenagel condensations. Reaction conditions: (a) Pyridine or piperidine, in MeOH or EtOH at reflux for 12-48 h (see the supporting information for more details).

a benzothiazolium moiety can now be obtained efficiently in a single step from compound **3** via a Knoevenagel condensation, affording the target dye in an excellent 99% yield (**5a**, Scheme 2). Building on this improved methodology, we extended the approach to the synthesis of a broader family of pCp-based cyanines incorporating oxygen- and selenium-containing heterocycles (**5b** and **5c**, Scheme 2), as well as pyridinium moieties (**5e** and **5f**, Scheme 2). The benzene-based analogs (**7a–f**, Scheme 2) were likewise synthesized using this strategy from commercially available aldehyde **6**, affording the "flat" dyes in yields ranging from 56% to 95%. The precursors required to perform the Knoevenagel condensations (**4a–f**, Scheme 2) were conveniently prepared via *N*-methylation of the corresponding neutral heterocycles (see Supporting Information for details).

Finally, a *para*-disubstituted pCp-based cyanine bearing a benzimidazolium motif (**5d**, Scheme 3) was successfully synthesized; however, the preparation of this molecule still required a two-step sequence consisting of a Horner–Wadsworth–Emmons reaction, followed by methylation (Scheme 3).

We then shifted our focus to the synthesis of a *pseudo-para*-disubstituted cyanine derived from [2.2]paracyclophane. To obtain this molecule, key aldehyde **14** was first prepared, showing a dimethylamino moiety on one aromatic ring of the pCp scaffold and a formyl group on the other (Scheme 4). The synthesis began with commercially available dibromide **9**, which was subjected to a lithium/halogen exchange, followed by the addition of DMF to introduce a formyl group through a substitution reaction. The resulting aldehyde **10** was protected as an acetal, then subjected to a Buchwald–Hartwig coupling with Boc-carbamate, affording product **12** in 46% overall yield. The Boc-protecting group was reduced using lithium aluminum hydride, generating methylamine **13** in an unoptimized 36% yield. Methylation at the nitrogen atom was then performed, followed by acetal deprotection, ultimately leading to the isolation of aldehyde **14** with a 9% overall yield across six steps. Knoevenagel condensation between this key compound and benzothiazolium derivative **4a** successfully afforded cyanine **15a**, with a yield of 42% (Scheme 4).

2.2 | Photophysical Characterization

The photophysical properties of the synthesized cyanines were investigated in both an organic solvent (dichloromethane) and an aqueous buffer (Tris-EDTA, TE), with 1% DMSO added to the buffer to ensure full solubilization of the dyes. Copies of the recorded spectra are reported in the supporting information (Figures S1–S39). A general trend observed for all compounds was a slight blueshift in both absorption and emission maxima when transitioning from the organic solvent to the aqueous medium (Table 1). Extinction coefficients and quantum yields were lower in the TE buffer compared to dichloromethane, indicating a reduction in the brightness ($B = \varepsilon \times \phi_f$) of the molecules in the more polar environment (off-state of the fluorogenic probes). The benzimidazolium and benzoxazolium derivatives exhibited more blueshifted bands compared to the analogous systems incorporating sulfur or selenium atoms (**5d**, **5b**, and **7d**, **7b** vs. **5a**, **5c**, and **7a**, **7c**; Table 1). The observed trend (more blueshifted = N < O < S < Se = more redshifted) can be explained

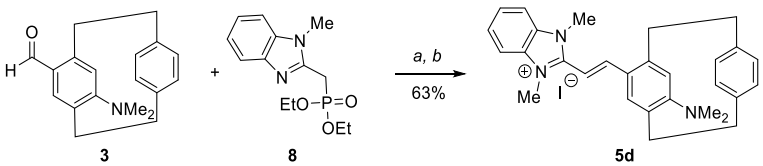

SCHEME 3 | Two-step procedure affording product **5d**. Reaction conditions: (a) NaH (2.0 equiv.), THF, 0°C to rt, 24 h; (b) MeI (4.0 equiv.), DMF, 100°C, 48 h.

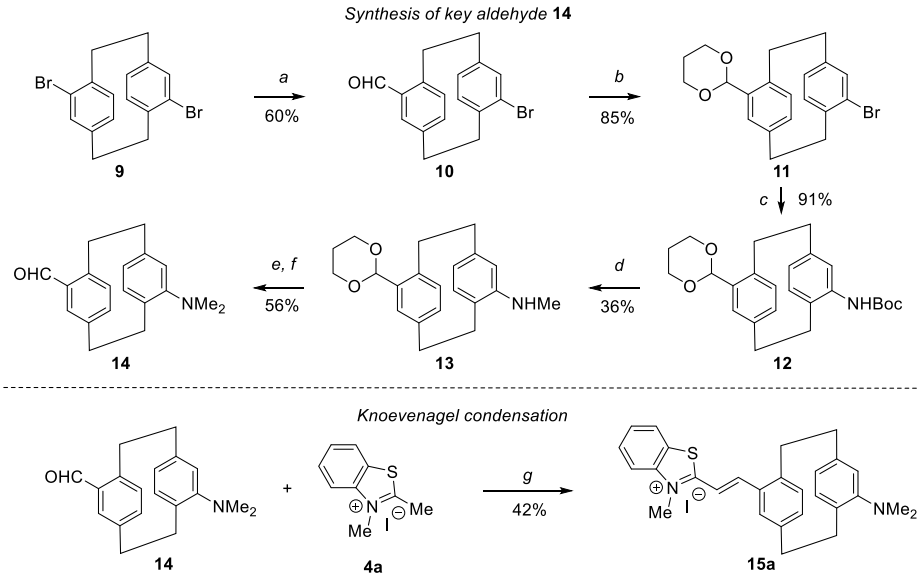

SCHEME 4 | Synthesis of compound **15a**. Reaction conditions: (a) *n*-BuLi (1.47 equiv.), THF, −78°C, 30 min; then DMF (8.09 equiv.), rt, 24 h; (b) $CH(OCH_3)_3$ (1.3 equiv.), 1,3-propanediol (5 equiv.), NBS (0.05 equiv.), MeOH (5 equiv.), rt, 24 h; (c) $BocNH_2$ (3 equiv.), Pd_2dba_3 (1 mol%), JohnpPhos (5 mol%), PhONa (3.6 equiv.), Toluene, 80°C, 20 h; (d) $LiAlH_4$ (1 equiv.), THF, 0°C to 80°C, 4 h; (e) MeI (1.3 equiv.), NaH (1.3 equiv.), DMF, rt, 24 h; (f) PTSA (0.09 equiv.), acetone/H_2O (1:1), rt, 24 h; (g) Pyridine (1.5 equiv.), MeOH, reflux, 60 h.

by considering the different electronegativity of the heteroatoms. Oxygen, being more electronegative than nitrogen, exerts a stronger electron-withdrawing effect on the charged heterocyclic moiety in the oxygenated dyes compared to the nitrogenated ones. Although sulfur and selenium have lower electronegativity than oxygen and nitrogen, their larger contribution to the orbital composition can induce smaller HOMO–LUMO gaps [36], which results in a bathochromic shift in the absorption and emission bands. The increased polarizability of sulfur and selenium compared to oxygen may also help stabilize the excited states of the dyes, further reducing the energy required for electronic transitions. Among both the pCp-based and pCp-deprived cyanines, the benzimidazolium (**5d** and **7d**, Table 1) and pyridinium (**5e**, **5f**, and **7e**, **7f**, Table 1) derivatives exhibited the largest Stokes shifts within the series of dyes, with this phenomenon being even more pronounced in TE buffer than in dichloromethane. The absorption and emission profiles of all *para*-disubstituted pCp dyes (**5a–f**, Table 1) were significantly redshifted compared to the analogous "flat" cyanines (**7a–f**, Table 1). This behavior, previously observed in other classes of fluorophores derived from [2.2]paracyclophane [37–39], is attributed to the presence of the second aromatic ring on the pCp core, which acts as a mild electron-donating substituent. Compound **5d** (Table 1) exhibited a significantly lower extinction coefficient in TE buffer compared to the other cyanines, possibly due to solubility issues in the aqueous medium, despite the use of DMSO as a cosolvent during the analyses. It is important to note that the pCp scaffold increases the lipophilic character of the dyes relative to the pCp-deprived cyanines. Lastly, absorption bands in the violet region were observed for the *pseudo-para*-disubstituted pCp dye **15a** (Table 1), but no fluorescence emission could be detected. Since compound **15a** exhibits photophysical properties similar to those of an analogous pCp system (**S4**) lacking the dimethylamino group (see Supporting Information for details, Figures S19–S21), the absence of fluorescence is attributed to insufficient through-space delocalization [40–42] between the electron-donating and electron-withdrawing groups attached to the two rings of the pCp core. Nonradiative decay processes may also be favored over radiative ones in this molecule.

2.3 | Fluorescence Enhancement Studies

In our previous work [34], we found that compound **5a** showed a significant fluorescence turn-on response upon interaction with Baker's yeast tRNA (*S. cerevisiae*). Titrating tRNA (0–2 mg) into a 1 μM solution of the pCp-based cyanine **5a** in TE buffer led to a ≈50-fold fluorescence enhancement (Figure 2). RNA denaturation and digestion experiments confirmed that this fluorescence increase occurs exclusively in the presence of the biomolecule in solution [34]. X-ray analysis of dye **5a**, together with NMR studies and UV–Vis titrations in the presence of increasing amounts of tRNA (see Figures S46, S52, S65, and S66 in the Supporting Information), suggests that the observed fluorescence enhancement likely arises from disaggregation processes induced by the interaction of the pCp-cyanine with RNA. We also conducted a selectivity study to compare the fluorescence turn-on responses of cyanine **5a** with its pCp-deprived analog, **7a**. Interestingly, while the flat dye **7a** showed similar high fluorescence enhancements when interacting with various nucleic acids (DNA, rRNA, tRNA), the three-dimensional pCp cyanine **5a** exhibited a fluorescence response that varied significantly depending on the type of nucleic acid it interacted with. In particular, we observed a minimal fluorescence turn-on with double-stranded DNA, while the greatest fluorescence enhancement was achieved with tRNA, which contains several unpaired motifs in its structure [43, 44].

We therefore expanded the selectivity study to include all the synthesized cyanines, aiming to compare their behavior based on the type of heterocyclic moiety introduced into the molecules (Figure 3). All measurements were conducted in TE buffer at 20°C, with 1% DMSO as a cosolvent to ensure complete solubilization of the dyes. Although the addition of DMSO did not

TABLE 1 | Photophysical properties of cyanines **5a–f**, **7a–f**, and **15a** in CH_2Cl_2 and TE buffer.

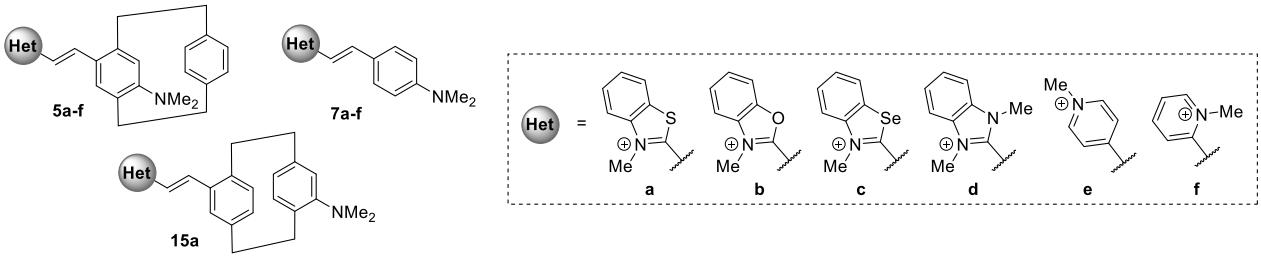

Dye[a]	Solvent	λ_{abs}^{max} (nm)	ε_{max} ($M^{-1}\cdot cm^{-1}$)	λ_{em}^{max} (nm)	$\Delta\lambda$ (nm)	ϕ_f (%)[b]	B ($M^{-1}\cdot cm^{-1}$)
5a	CH_2Cl_2	597	46 000	645	48	2.0	920
	TE[c]	565	39 000	635	70	1.5	585
5b	CH_2Cl_2	561	57 000	607	46	3.8	2166
	TE[c]	540	36 000	599	59	1.2	432
5c	CH_2Cl_2	606	55 000	653	47	1.2	660
	TE[c]	580	15 000	642	62	0.7	105
5d	CH_2Cl_2	474	45 000	618	144	3.0	1,350
	TE[c]	424	5500	579	155	7.3	413
5e	CH_2Cl_2	566	21 000	645	79	3.7	777
	TE[c]	485	15 000	632	147	3.1	465
5f	CH_2Cl_2	542	42 000	630	88	4.3	1806
	TE[c]	472	15 000	611	139	2.3	345
7a	CH_2Cl_2	553	44 000	607	54	6.2	2728
	TE[c]	510	36 000	600	90	1.3	468
7b	CH_2Cl_2	522	54 000	569	47	5.9	3186
	TE[c]	488	35 000	563	75	2.3	805
7c	CH_2Cl_2	563	51 000	614	51	2.6	1326
	TE[c]	521	42 000	607	86	1.0	420
7d	CH_2Cl_2	440	12 000	544	104	3.1	372
	TE[c]	380	15 000	545	165	4.5	675
7e	CH_2Cl_2	523	32 000	610	87	32.6	10 432
	TE[c]	488	25 000	610	122	1.9	475
7f	CH_2Cl_2	504	20 000	593	89	30.5	6100
	TE[c]	438	20 000	584	146	2.9	580
15a	CH_2Cl_2	429	22 000	—	—	—	—
	TE	400	16 000	—	—	—	—

[a]10^{-5} M solutions.
[b]Absolute quantum yields.
[c]1% DMSO was added to fully solubilize the dyes. A comprehensive visual comparison of photophysical properties across the dye series is provided in Figures S40–S43 of the Supporting Information.

significantly alter the experimental results, slightly improved turn-on responses were observed in some cases due to enhanced dye solubility (see Figures S44 and S45 in the Supporting Information for further details). Under these conditions, the behaviors of cyanines **5a** and **7a** were successfully reproduced (Figure 3a). While investigating other pCp-based cyanines and their flat analogs, several interesting trends emerged. Although fluorescence enhancements varied depending on the heterocyclic moiety in the molecules, similar I_{max}/I_0 values were observed for compounds **7b**, **7c**, **7e**, and **7f** (Figure 3) in the presence of tRNA (*S. cerevisiae*), DNA (from calf thymus), or total RNA from Baker's yeast (primarily containing rRNA). Like compound **7a**, these flat cyanines appear to be nonselective, interacting similarly with various nucleic acids, and in some cases, even showing a preference for DNA over RNA. Curiously, dye **7d** exhibited a poor fluorescence turn-on response in all the experiments (Figure 3). This dye, however, exhibits higher quantum yields than its analogs in TE (Table 1), suggesting it may already be partially in the "on" state in this medium, a behavior that could explain the observed reduced relative enhancement in emission.

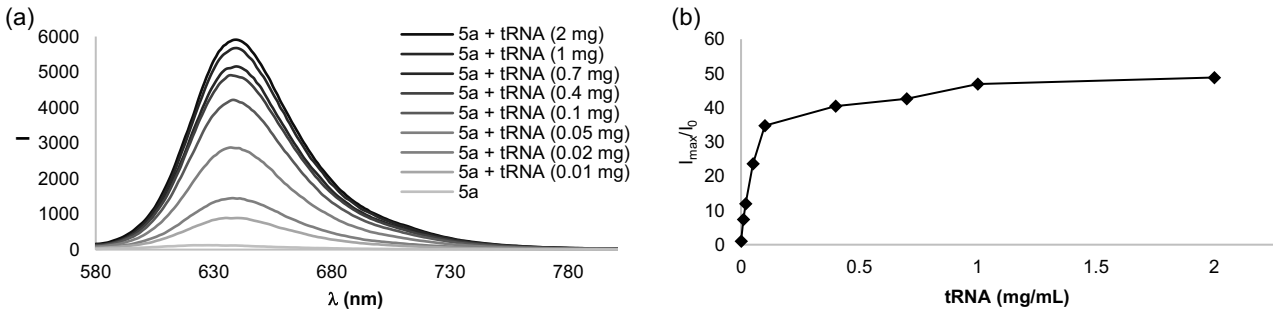

FIGURE 2 | (a) Representative fluorescence titration of pCp-based cyanine **5a** (10^{-6} M solution) with increasing quantities of Baker's yeast tRNA in a TE buffer at 20°C ($\lambda_{ex} = 550$ nm). (b) Plot of fluorescence intensity enhancement (I_{max}/I_0) of pCp-based cyanine **5a** (10^{-6} M solution) at 630 nm ($\lambda_{ex} = 550$ nm) in the presence of increasing quantities of Baker's yeast tRNA (0 to 2 mg/mL).

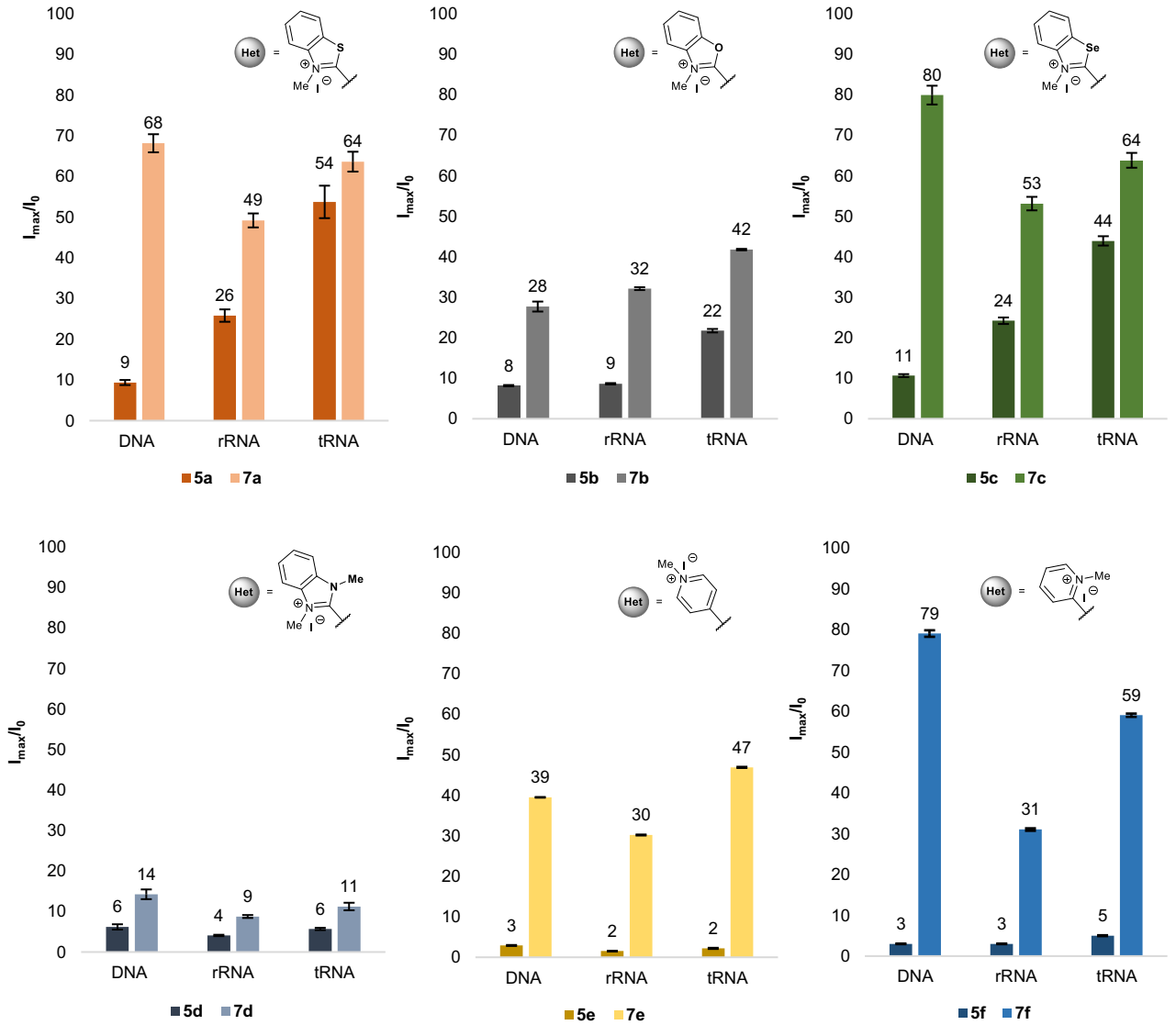

FIGURE 3 | Selectivity of cyanines **5a–f** or **7a–f** (1 μM) vs. different species of nucleic acids (0.5 mg/mL) in a TE buffer at 20°C. 1% DMSO was added as cosolvent to perform all the measures. Experiments were performed in triplicate (error bar: mean standard deviation). Fluorescence intensity enhancement (I_{max}/I_0) were recorded at each dye's maximum emission, with excitation at the corresponding maximum absorption (for more information, see the supporting information, Tables S1 and S3).

For the pCp-based cyanines featuring benzoxazolium and benzoselenazolium moieties (**5b** and **5c**, Figure 3), increased selectivity was observed compared to their flat analogs, as previously noted for dye **5a**. Indeed, low fluorescence enhancements were recorded for the three-dimensional molecules in the presence of double-stranded DNA, while significantly stronger responses

were detected with tRNA. These findings emphasize the preferential interaction of these pCp-based compounds with tRNA over DNA. In the presence of rRNA, the I_{max}/I_0 ratios for compounds **5a** and **5c** were lower than those observed with tRNA but higher than those seen with DNA (Figure 3). While rRNA contains unpaired regions, their limited accessibility may explain the reduced fluorescence emissions of **5a** and **5c** compared to tRNA, where these regions are more readily accessible for interaction [43, 44]. Similarly to **7d**, the 3D dyes-containing benzimidazolium and pyridinium moieties (**5d–f**, Figure 3) exhibit stronger emission in TE buffer compared to other pCp-based cyanines, as highlighted by their higher quantum yields in the aqueous medium (Table 1). Intrinsically more intense fluorescence may again partly account for the low I_{max}/I_0 values observed for these nitrogen-containing dyes, as they are already partially "turned on" even in the absence of nucleic acids. These results therefore suggest that benzimidazolium and pyridinium motifs are less suitable for the development of fluorogenic RNA ligands within this series of 3D cyanine dyes.

X-ray analysis of the synthesized pCp-derivatives highlighted that compounds **5a** and **5b** display similar crystallization patterns, with two molecules in a head-to-tail arrangement [45]. The other molecules exhibit different packing profiles in the solid state (see the supporting information for more details, Figures S65–S74). This feature, along with NMR analyses, indicating that all synthesized compounds form aggregates with potentially distinct disaggregation behaviors in solution (see Supporting Information for details, Figures S46–S51), may partly explain the reduced turn-on response observed for certain dyes.

Finally, it is worth noting that a fluorescence enhancement study was performed with the *pseudo-para*-substituted dye **15a** in the presence of increasing quantities of tRNA (up to 2 mg/mL); however, no turn-on response was observed. This finding further supports the hypothesis that insufficient through-space conjugation occurs between the cationic heterocyclic moiety and the dimethylamino group in this system, as these groups are located on opposite rings of the pCp core. Consequently, it is unlikely that analogs of this compound would function as effective fluorogenic RNA binders within this molecular family.

2.4 | Binding Interactions with RNA Hairpin Loops

In our previous study [34], we investigated the turn-on response of pCp-based cyanine **5a** in the presence of structured single-stranded RNA sequences of varying lengths. Fluorescence titrations were conducted to evaluate the interaction between dye **5a** and tetra-, hexa-, octa-, or deca-hairpin loop structures (see Figures S54, S56–58, S61, and S63 in the Supporting Information). Cyanine **5a** displayed a strong affinity and selectivity for larger loops, with the highest preference for the octa-loop sequence **C**. The dissociation constant for this sequence ($K_d \approx 0.5\,\mu M$) was about threefold lower than for loop **D**, 15-fold lower than for loop **B**, and up to 60-fold lower than for loop **A** (Table 2).

To compare the fluorescence enhancement exhibited by **5a** with that of the newly synthesized cyanines **5b–f**, turn-on experiments were performed using the same set of RNA hairpin loops. While the luminescence of compounds **5b**, **5d**, **5e**, and **5f** was largely unaffected by the different RNA sequences, dyes **5a** and **5c** showed similar trends, indicating that the benzoselenazolium derivative **5c** behaves comparably to the benzothiazolium compound **5a**, with preferential interactions toward larger hairpin loops.

Indeed, at a 1:1 dye/RNA ratio, I_{max}/I_0 values of up to ≈12 were observed in the presence of loops **C** and **D**, whereas only a fivefold increase was detected for loop **B** and no turn-on was observed for loop **A** (Figure 4). It is worth noting that the apparent difference in the turn-on response between loops **C** and **D** for **5a** ($I_{max}/I_0 = 12$ vs. 15) is not statistically significant when the associated error bars are taken into account (Figure 4). To complement these turn-on experiments and quantify the interactions of **5c** with the RNA hairpin loops, dissociation constants (K_d) were measured for the same sequences via fluorescence titrations (see Supporting Information, Figures S55, S59, S60, and S62). Binding trends comparable to those observed for **5a** were found (Table 2), with preferential interaction with the larger loops **C** and **D** ($K_d \approx 5\,\mu M$), a twofold reduction in affinity for loop **B** ($K_d \approx 13\,\mu M$), and no significant interaction with the smallest loop **A**. Overall, the K_d values for **5c** were higher than those of **5a**, indicating weaker interactions with the RNA targets.

TABLE 2 | Dissociation constants (K_d, μM) for the interaction of various RNA hairpin loops with cyanines **5a** and **5c**.

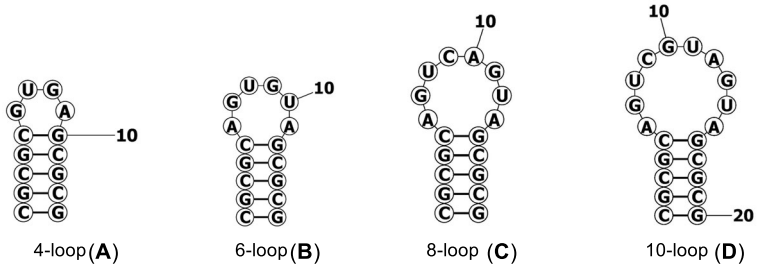

Dye[a]	4-loop (A)	6-loop (B)	8-loop (C)	10-loop (D)
5a	24.5 ± 6.6	6.04 ± 2.05	0.54 ± 0.16	1.65 ± 1.14
5c	>50	13.38 ± 3.07	5.06 ± 1.23	5.36 ± 0.73

[a]Titrations were performed with 10^{-6} M solutions of the dyes in TE for loops **A** and **B**, 10^{-7} M solutions of the dyes in TE for loops **C** and **D.** Experiments were performed in triplicate (error bar: mean standard deviation). For more information, see the supporting information (Figures S54–S63).

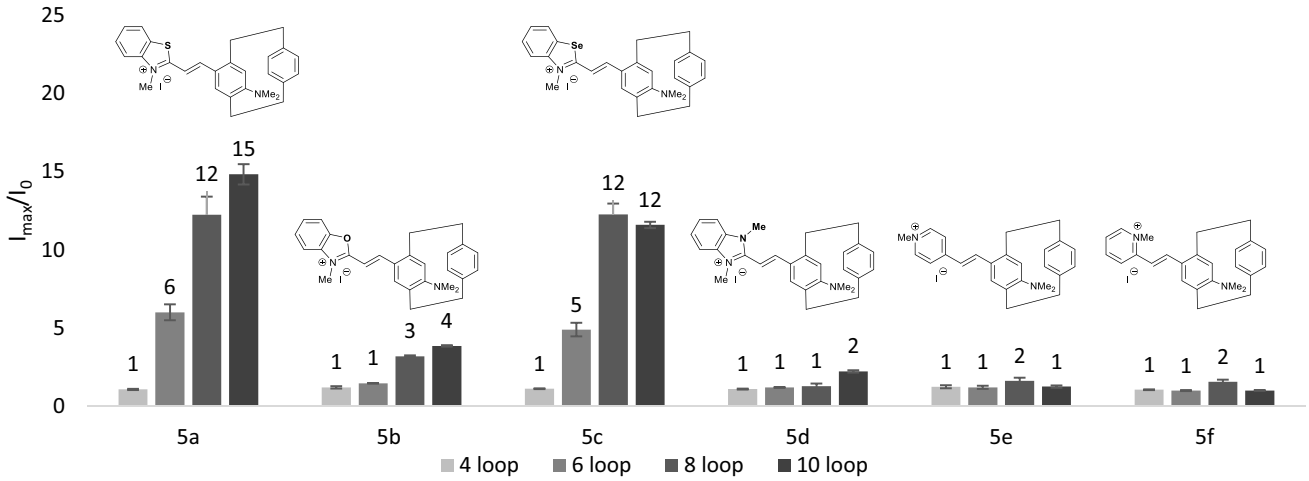

FIGURE 4 | Selectivity of cyanines **5a–f** (1 μM) versus different RNA loops (1 μM) in a TE buffer at 20°C. 1% DMSO was added as cosolvent to perform all the measures. Experiments were performed in triplicate (error bar: mean standard deviation). The plots of fluorescence intensity enhancement (I_{max}/I_0) were recorded at each dye's maximum emission, with excitation at the corresponding maximum absorption (for more information, see the supporting information, Table S2).

Nevertheless, the loop-size-dependent binding pattern remains preserved for this compound. The consistency between the turn-on responses and the binding data indicate that the molecular features of the dyes play a key role in governing their responses. In particular, the similar behavior of the benzothiazolium and benzoselenazolium dyes likely reflects their soft, polarizable character, which can enhance dispersion-driven interactions with unpaired nucleobases. In contrast, the lower polarizability of the benzoxazolium, benzimidazolium, and pyridinium analogs may contribute to their reduced turn-on responses in the presence of RNA. As mentioned earlier, these compounds may also tend to form aggregates, which could be more stable in aqueous solution and thus dissociate less readily upon interaction with nucleic acids.

To gain deeper insight into the interaction mode of the pCp-based cyanines with 8-loop **C**, circular dichroism (CD) experiments were performed. As shown in Figure 5a, the addition of increasing amounts of racemic compound **5a** (up to

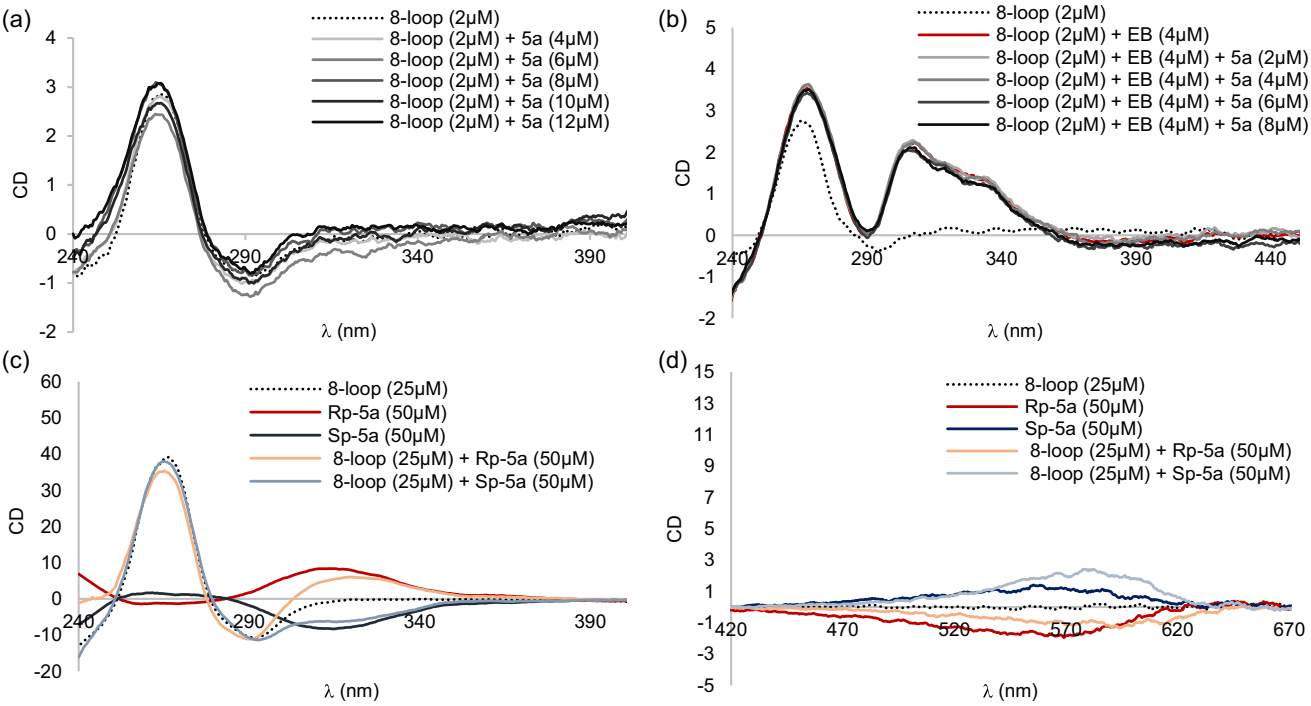

FIGURE 5 | (a) Circular dichroism signatures in a TE buffer of RNA 8-loop **C** (2 μM) with increasing amount of racemic pCp cyanine **5a** (up to 6 equiv.). (b) Circular dichroism signatures in a TE buffer of RNA 8-loop **C** (2 μM), RNA 8-loop **C** (2 μM) and ETB (4 μM), and RNA 8-loop **C** (2 μM) and ETB (4 μM) with increasing amount of racemic pCp cyanine **5a** (up to 4 equiv.). (c) Circular dichroism signatures in a TE buffer, between 240 and 390 nm, of RNA 8-loop **C** (25 μM), R_p-**5a** or S_p-**5a** (50 μM), and the corresponding mixtures. (d) Circular dichroism signatures in a TE buffer, between 420 and 670 nm, of RNA 8-loop **C** (25 μM), R_p-**5a** or S_p-**5a** (50 μM), and the corresponding mixtures.

6 equivalents) to loop **C** induced no significant changes in the CD signature of the helix at 260 nm, which arises from Watson–Crick base pairing. This observation suggests that the pCp-based cyanine does not interact with the double-helical region of the RNA sequence.

To corroborate the hypothesis that dye **5a** does not intercalate into the double-helical region of loop **C**, a competitive displacement experiment was conducted in the presence of ethidium bromide (EB), a well-known nucleic-acid intercalator. As shown in Figure 5b, the addition of two equivalents of EB to 8-loop **C** produced a clear increase in the magnitude of the positive Cotton effect around 260 nm, a result typically associated with tighter base stacking and altered electronic coupling resulting from intercalation. In addition, new CD bands (a positive ICD at 320–330 nm) emerged. This spectral signature is characteristic of ethidium bromide, which, although achiral, acquires induced optical activity when intercalated between the chiral bases of RNA [46]. When increasing amounts of dye **5a** (up to 4 equivalents) were added to the solution containing 8-loop **C** and EB, no changes in the CD signatures were observed, indicating that dye **5a** does not displace EB and is likely binding to a different region of the hairpin loop (Figure 5b).

Next, the effect of RNA 8-loop **C** (0.5 equiv.) on the CD spectra of both enantiomers of cyanine **5a**, synthesized from enantiopure aldehyde **3**, was examined. As shown in Figure 5c,d, distinct changes in the CD signals of the cyanine dyes near 310 and 570 nm confirm the occurrence of RNA–dye interactions. In particular, the presence of loop **C** induces a red shift in the CD maximum of the pCp-based compounds R_p-**5a** and S_p-**5a** from 570 to 590 nm (Figure 5d), indicating an alteration in the dye environment upon binding. In contrast, the CD band at 260 nm, characteristic of the RNA helical structure (Figure 5c) [47, 48], remains unaltered, confirming that the 8-loop RNA helix is not perturbed. Altogether, the results of these CD studies support the hypothesis that the sterically hindered pCp dye **5a** does not intercalate into double-helical regions but instead preferentially associates with the unpaired loop motif of the RNA.

To further examine how the topology of the 8-loop **C** motif governs dye recognition, we performed molecular docking of both R_p-**5a** and S_p-**5a** against an ensemble of 20 three-dimensional RNA loop conformations. Only a subset of these structures displayed an internal cavity capable of accommodating the pCp ligand, and these permissive geometries were characterized by transient widening of the loop interior. In a representative conformation, both enantiomers docked within the loop-facing pocket; however, the S_p enantiomer adopted a more compact and energetically favorable orientation (Figure 6).

Across the full ensemble, S_p-**5a** more frequently sampled low-penalty poses, whereas R_p-**5a** achieved a comparable fit in only a single model (see the supporting information for more details, Table S20). These results support the experimental observations and suggest that the RNA loop may provide a chiral environment capable of influencing enantiomer orientation, with loop geometry serving as a key determinant of dye recognition.

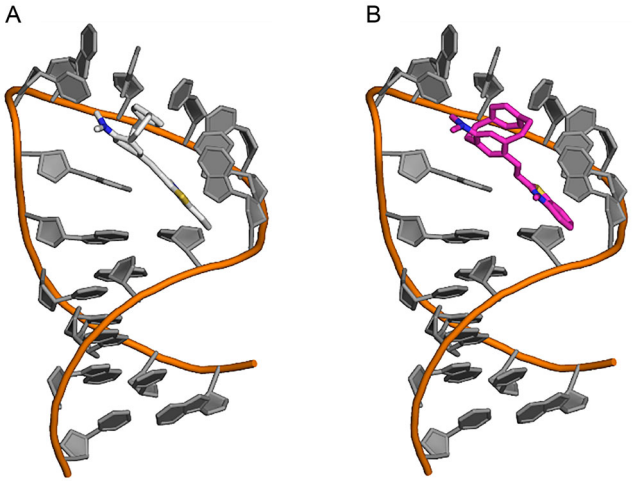

FIGURE 6 | Docking of (A) S_p-**5a** and (B) R_p-**5a** in a representative 8-loop **C** RNA conformation.

3 | Conclusion

In conclusion, we have synthesized a series of [2.2]paracyclophane-based three-dimensional cyanines. Their photophysical properties were characterized and compared to those of analogous "flat" cyanine dyes lacking the pCp unit. Heteroatom variation, as well as heterocycle modification, proved to strongly impact the turn-on properties of the pCp dyes. We investigated the interaction of all synthesized compounds with various types of nucleic acids and found that the 3D benzothiazole- and benzoselenazole-containing derivatives retain the turn-on fluorescence behavior of their flat counterparts, while displaying improved selectivity toward RNAs-containing unpaired structural motifs. Furthermore, our results indicate that these pCp-derived molecules preferentially bind to large RNA hairpin loops. CD studies indicate that binding does not involve intercalation into double-helical regions, and molecular docking suggests that loop geometry is a key determinant of dye recognition. At this stage, the observed selectivity trend has been demonstrated only for this series of 3D paracyclophane derivatives and may be specific to the cyanine backbone. Studies are ongoing in our laboratory to clarify the binding mechanism of pCp-based cyanines with more complex RNA architectures and to evaluate whether the shape-modifying strategy described in this article can be generalized to other classes of RNA-binding dyes.

Acknowledgments

The authors gratefully acknowledge the CNRS and Université Paris Cité for their financial support. This work has received support under the program "*Investissement d'Avenir*" launched by the French Government and implemented by ANR, with the reference "*ANR-21-EXES-0002*, *FIRE-UP*" as part of its program "*CCE*" (3DRNA project). The authors sincerely thank P. Hardouin and B. Sargueil for their assistance with fluorescence turn-on measurements involving RNA hairpin loops, and J. Boissieras and A. Granzhan for their help with CD measurements and insightful discussions. The authors also wish to acknowledge M. Chamoreau (Plateforme Diffraction X, IPCM, Sorbonne Université) and P. Gerardo (Plateforme de Spectrométrie de Masse, LCBPT, Université Paris Cité) for their valuable help with X-ray crystallography and mass spectrometry analysis.

Conflicts of Interest

The authors declare no conflicts of interest.

Data Availability Statement

The data that support the findings of this study are available from the corresponding author upon reasonable request.

References

1. F. Crick, "Central Dogma of Molecular Biology," *Nature* 227 (1970): 561.

2. H. P. Yockey, *Information Theory, Evolution, and the Origin of Life* (Cambridge University Press, 2005), 20.

3. K. D. Warner, C. E. Hajdin, and K. M. Weeks, "Principles for Targeting RNA with Drug-Like Small Molecules," *Nature Reviews Drug Discovery* 17 (2018): 547.

4. L. Poliseno, M. Lanza, and P. P. Pandolfi, "Coding, or Non-Coding, that is the Question," *Cell Research* 34 (2024): 609.

5. K. Nemeth, R. Bayraktar, M. Ferracin, and G. A. Calin, "Non-Coding RNAs in Disease: From Mechanisms to Therapeutics," *Nature Reviews. Genetics* 25 (2024): 211.

6. C. M. Connelly, M. H. Moon, and J. S. Schneekloth, "The Emerging Role of RNA as a Therapeutic Target for Small Molecules," *Cell Chemical Biology* 23 (2016): 1077.

7. C. R. Fullenkamp, X. Liang, M. Pettersson, and J. Schneekloth Jr, *RNA as a Drug Target* (John Wiley & Sons, Ltd., 2024), 355.

8. J. P. Falese, A. Donlic, and A. E. Hargrove, "Targeting RNA with Small Molecules: From Fundamental Principles towards the Clinic," *Chemical Society Reviews* 50 (2021): 2224.

9. T. C. Roberts, R. Langer, and M. J. A. Wood, "Advances in Oligonucleotide Drug Delivery," *Nature Reviews. Drug Discovery* 19 (2020): 673.

10. C. F. Bennett, "Therapeutic Antisense Oligonucleotides Are Coming of Age," *Annual Review of Medicine* 70 (2019): 307.

11. M. C. Lauffer, W. van Roon-Mom, and A. Aartsma-Rus, "Possibilities and Limitations of Antisense Oligonucleotide Therapies for the Treatment of Monogenic Disorders," *Communication & Medicine* 4 (2024): 6.

12. X. Chi, P. Gatti, and T. Papoian, "Safety of Antisense Oligonucleotide and siRNA-Based Therapeutics," *Drug Discovery Today* 22 (2017): 823.

13. L. Guan and M. D. Disney, "Recent Advances in Developing Small Molecules Targeting RNA," *ACS Chemical Biology* 7 (2012): 73.

14. S. Kovachka, M. Panosetti, B. Grimaldi, S. Azoulay, A. Di Giorgio, and M. Duca, "Small Molecule Approaches to Targeting RNA," *Nature Reviews Chemistry* 8 (2024): 120.

15. J. L. Childs-Disney, X. Yang, Q. M. R. Gibaut, Y. Tong, R. T. Batey, and D. M., "Disney Targeting RNA Structures with Small Molecules," *Nature Reviews. Drug Discovery* 21 (2022): 736.

16. H. Ratni, R. S. Scalco, and A. H. Stephan, "Risdiplam, the First Approved Small Molecule Splicing Modifier Drug as a Blueprint for Future Transformative Medicines," *ACS Medicinal Chemistry Letters* 12 (2021): 874.

17. S. Ramdas and L. Servais, "New Treatments in Spinal Muscular Atrophy: An Overview of Currently Available Data," *Expert Opinion on Pharmacotherapy* 21 (2020): 307.

18. S. Chen, Q. Mao, H. Cheng, and W. Tai, "RNA-Binding Small Molecules in Drug Discovery and Delivery: An Overview From Fundamentals," *Journal of Medicinal Chemistry* 67 (2024): 16002.

19. H. Ratni, M. Ebeling, J. Baird, et al., "Discovery of Risdiplam, a Selective Survival of Motor Neuron-2 (SMN2) Gene Splicing Modifier for the Treatment of Spinal Muscular Atrophy (SMA)," *Journal of Medicinal Chemistry* 61 (2018): 6501.

20. A. Umuhire Juru and A. E. Hargrove, "Frameworks for Targeting RNA with Small Molecules," *The Journal of Biological Chemistry* 296 (2021): 100191.

21. A. E. Hargrove, "Small Molecule–RNA Targeting: Starting with the Fundamentals," *Chemical Communications* 56 (2020): 14744.

22. S. T. Meyer and P. J. Hergenrother, "Small Molecule Ligands for Bulged RNA Secondary Structures," *Organic Letters* 11 (2009): 4052.

23. S. A. Barros and D. M. Chenoweth, "Triptycene-Based Small Molecules Modulate (CAG)·(CTG) Repeat Junctions," *Chemical Science* 6 (2015): 4752.

24. S. A. Barros and D. M. Chenoweth, "Recognition of Nucleic Acid Junctions Using Triptycene-Based Molecules," *Angewandte Chemie International Edition* 53 (2014): 13746.

25. S. A. Barros, I. Yoon, and D. M. Chenoweth, "Modulation of the E. Coli rpoH Temperature Sensor with Triptycene-Based Small Molecules," *Angewandte Chemie International Edition* 55 (2016): 8258.

26. L. Melidis, H. J. Hill, N. J. Coltman, et al., "Organometallic Pillarplexes That Bind DNA. 4-Way Holliday Junctions and Forks," *Angewandte Chemie International Edition* 133 (2021): 18292.

27. S. Phongtongpasuk, S. Paulus, J. Schnabl, et al., "Binding of a Designed Anti-Cancer Drug to the Central Cavity of an RNA Three-Way Junction," *Angewandte Chemie International Edition* 52 (2013): 11513.

28. C. Fleurisson, N. Graidia, J. Azzouz, et al., "Design and Evaluation of Azaspirocycles as RNA Binders," *Chemistry: A European Journal* 31 (2025): e202403518.

29. E. Benedetti and L. Micouin, "Have Spirocyclic Scaffolds Been Properly Utilized in Recent Drug Discovery Efforts?," *Expert Opinion on Drug Discovery* 19 (2024): 263.

30. N. Akbay, M. Yu Losytskyy, V. B. Kovalska, A. O. Balanda, and S. M. Yarmoluk, "The Mechanism of Benzothiazole Styrylcyanine Dyes Binding with dsDNA: Studies by Spectral-Luminescent Methods," *Journal of Fluorescence* 18 (2008): 139.

31. V. B. Kovalska, D. V. Kryvorotenko, A. O. Balanda, M. Yu Losytskyy, V. P. Tokar, and S. M. Yarmoluk, "Fluorescent Homodimer Styrylcyanines: Synthesis and Spectral-Luminescent Studies in Nucleic Acids and Protein Complexes," *Dyes and Pigments* 67 (2005): 47.

32. C.-Q. Zhu, S.-J. Zhuo, H. Zheng, et al., "Fluorescence Enhancement Method for the Determination of Nucleic Acids Using Cationic Cyanine as a Fluorescence Probe," *The Analyst* 129 (2004): 254.

33. C. J. Brown and A. C. "Farthing, "Preparation and Structure of Di-p-Xylylene," *Nature* 164 (1949): 915.

34. S. Felder, C. Sagné, E. Benedetti, and L. Micouin, "Small-Molecule 3D Ligand for RNA Recognition: Tuning Selectivity through Scaffold Hopping," *ACS Chemical Biology* 17 (2022): 3069.

35. S. Felder, L. Micouin, and E. Benedetti, "Para-Functionalization of N-Substituted 4-Amino[2.2]paracyclophanes by Regioselective Formylation," *European Journal of Organic Chemistry* 2021 (2021): 4015.

36. S. Riebe, C. Wölper, J. Balszuweit, et al., "Understanding the Role of Chalcogens in Ether-Based Luminophores with Aggregation-Induced Fluorescence and Phosphorescence," *ChemPhotoChem* 4 (2020): 398.

37. E. Benedetti, M.-L. Delcourt, B. Gatin-Fraudet, S. Turcaud, and L. Micouin, "Synthesis and Photophysical Studies of through-Space Conjugated [2.2]paracyclophane-Based Naphthalene Fluorophores," *RSC Advances* 7 (2017): 50472.

38. M.-L. Delcourt, C. Reynaud, S. Turcaud, et al., "3D Coumarin Systems Based on [2.2]Paracyclophane: Synthesis, Spectroscopic Characterization, and Chiroptical Properties," *The Journal of Organic Chemistry* 84 (2019): 888.

39. S. Felder, M.-L. Delcourt, M. H. E. Bousquet, et al., "Planar Chiral Analogues of PRODAN Based on a [2.2]Paracyclophane Scaffold: Synthesis and Photophysical Studies," *The Journal of Organic Chemistry* 87 (2022): 147.

40. S. Felder, M.-L. Delcourt, R. Rodríguez, et al., "Compact CPL Emitters Based on a [2.2]paracyclophane Scaffold: Recent Developments and Future Perspectives," *Journal of Materials Chemistry C* 11 (2023): 2053.

41. Z. Hassan, E. Spuling, D. M. Knoll, J. Lahann, and S. Bräse, "Planar Chiral [2.2]paracyclophanes: From Synthetic Curiosity to Applications in Asymmetric Synthesis and Materials," *Chemical Society Reviews* 47 (2018): 6947.

42. S. Wu, S. Felder, F. Pointillart J.Brom, O. Maury, L. Micouin, and E. Benedetti, "[2.2]Paracyclophanes: From Selective Functionalization to Optical Properties," *Advanced Optical Materials* 12 (2024): 2400934.

43. Q. Vicens and J. S. Kieft, "Thoughts on How to Think (and Talk) about RNA Structure," *Proceedings of the National Academy of Sciences of the United States of America* 119 (2022): e2112677119.

44. J. C. Lee and R. R. Gutell, "Diversity of Base-Pair Conformations and Their Occurrence in rRNA Structure and RNA Structural Motifs," *Journal of Molecular Biology* 344 (2004): 1225.

45. *Crystallographic data for* ***5a-c*** *and* ***5e,f*** *has been deposited at the CCDC under [2465406-2465410] and can be obtained from* https://www.ccdc.cam.ac.uk.

46. S. Parodi, F. Kendall, and C. Nicolini, "A Clarification of the Complex Spectrum Observed with the Ultraviolet Circular Dichroism of Ethidium Bromide Bound to DNA," *Nucleic Acids Research* 2 (1975): 477.

47. J. Kypr, I. Kejnovská, D. Renčiuk, and M. Vorlíčková, "Circular Dichroism and Conformational Polymorphism of DNA," *Nucleic Acids Research* 37 (2009): 1713.

48. J. A. Jaeger, J. SantaLucia Jr., and I. Tinoco Jr, "Determination of RNA Structure and Thermodynamics," *Annual Review of Biochemistry* 62 (1993): 255.

Supporting Information

Additional supporting information can be found online in the Supporting Information section. **Supporting Fig. S1:** (a) UV-Vis absorption of **5a** in CH_2Cl_2 (10^{-5} M solution); (b) UV-Vis absorption of **5a** in absorption in TE + 1% DMSO (10^{-5} M solution). **Supporting Fig. S2:** (a) Fluorescence emission of **5a** in CH_2Cl_2 (10^{-5} M solution, $\lambda_{ex} = 600$); (b) Fluorescence emission of **5a** in absorption in TE + 1% DMSO (10^{-5} M solution, $\lambda_{ex} = 595$). **Supporting Fig. S3:** (a) Normalized fluorescence emission of **5a** in CH_2Cl_2 (10^{-5} M solution, $\lambda_{ex} = 600$); (b) Normalized fluorescence emission of **5a** in absorption in TE + 1% DMSO (10^{-5} M solution, $\lambda_{ex} = 595$). **Supporting Fig. S4:** (a) UV-Vis absorption of **5b** in CH_2Cl_2 (10^{-5} M solution); (b) UV-Vis absorption of **5b** in absorption in TE + 1% DMSO (10^{-5} M solution). **Supporting Fig. S5:** (a) Fluorescence emission of **5b** in CH_2Cl_2 (10^{-5} M solution, $\lambda_{ex} = 560$); (b) Fluorescence emission of **5b** in absorption in TE + 1% DMSO (10^{-5} M solution, $\lambda_{ex} = 540$). **Supporting Fig. S6:** (a) Normalized fluorescence emission of **5b** in CH_2Cl_2 (10^{-5} M solution, $\lambda_{ex} = 560$); (b) Normalized fluorescence emission of **5b** in absorption in TE + 1% DMSO (10^{-5} M solution, $\lambda_{ex} = 540$). **Supporting Fig. S7:** (a) UV-Vis absorption of **5c** in CH_2Cl_2 (10^{-5} M solution); (b) UV-Vis absorption of **5c** in absorption in TE + 1% DMSO (10^{-5} M solution). **Supporting Fig. S8:** (a) Fluorescence emission of **5c** in CH_2Cl_2 (10^{-5} M solution, $\lambda_{ex} = 600$); (b) Fluorescence emission of **5c** in absorption in TE + 1% DMSO (10^{-5} M solution, $\lambda_{ex} = 580$). **Supporting Fig. S9:** (a) Normalized fluorescence emission of **5c** in CH_2Cl_2 (10^{-5} M solution, $\lambda_{ex} = 600$); (b) Normalized fluorescence emission of **5c** in absorption in TE + 1% DMSO (10^{-5} M solution, $\lambda_{ex} = 580$). **Supporting Fig. S10:** (a) UV-Vis absorption of **5d** in CH_2Cl_2 (10^{-5} M solution); (b) UV-Vis absorption of **5d** in absorption in TE + 1% DMSO (10^{-5} M solution). **Supporting Fig. S11:** (a) Fluorescence emission of **5d** in CH_2Cl_2 (10^{-5} M solution, $\lambda_{ex} = 470$); (b) Fluorescence emission of **5d** in absorption in TE + 1% DMSO (10^{-5} M solution, $\lambda_{ex} = 420$). **Supporting Fig. S12:** (a) Normalized fluorescence emission of **5d** in CH_2Cl_2 (10^{-5} M solution, $\lambda_{ex} = 470$); (b) Normalized fluorescence emission of **5d** in absorption in TE + 1% DMSO (10^{-5} M solution, $\lambda_{ex} = 420$). **Supporting Fig. S13:** (a) UV-Vis absorption of **5e** in CH_2Cl_2 (10^{-5} M solution); (b) UV-Vis absorption of **5e** in absorption in TE + 1% DMSO (10^{-5} M solution). **Supporting Fig. S14:** (a) Fluorescence emission of **5e** in CH_2Cl_2 (10^{-5} M solution, $\lambda_{ex} = 560$); (b) Fluorescence emission of **5e** in absorption in TE + 1%DMSO (10^{-5} M solution, $\lambda_{ex} = 480$). **Supporting Fig. S15:** (a) Normalized fluorescence emission of **5e** in CH_2Cl_2 (10^{-5} M solution, $\lambda_{ex} = 560$); (b) Normalized fluorescence emission of **5e** in absorption in TE + 1% DMSO (10^{-5} M solution, $\lambda_{ex} = 480$). **Supporting Fig. S16:** (a) UV-Vis absorption of **5f** in CH_2Cl_2 (10^{-5} M solution); (b) UV-Vis absorption of **5f** in absorption in TE + 1%DMSO (10^{-5} M solution). **Supporting Fig. S17:** (a) Fluorescence emission of **5f** in CH_2Cl_2 (10^{-5} M solution, $\lambda_{ex} = 540$); (b) Fluorescence emission of **5f** in absorption in TE + 1% DMSO (10^{-5} M solution, $\lambda_{ex} = 470$). **Supporting Fig. S18:** (a) Normalized fluorescence emission of **5f** in CH_2Cl_2 (10^{-5} M solution, $\lambda_{ex} = 540$); (b) Normalized fluorescence emission of **5f** in absorption in TE + 1% DMSO (10^{-5} M solution, $\lambda_{ex} = 470$). **Supporting Fig. S19:** (a) UV-Vis absorption of **15a** in CH_2Cl_2 (10^{-5} M solution, $\lambda_{abs}^{max} = 429$ nm); (b) UV-Vis absorption of **15a** in absorption in TE + 1% DMSO (10^{-5} M solution, $\lambda_{abs}^{max} = 400$ nm). **Supporting Fig. S20:** (a) UV-Vis absorption of **S4** in CH_2Cl_2 (10^{-5} M solution, $\lambda_{abs}^{max} = 445$ nm); (b) UV-Vis absorption of **S4** in absorption in TE + 1% DMSO (10^{-5} M solution, $\lambda_{abs}^{max} = 410$ nm). **Supporting Fig. S21:** Comparison of UV-Vis absorption spectra of compounds of compounds **15a** and **S4** in TE + 1% DMSO (10^{-5} M solutions). **Supporting Fig. S22:** (a) UV-Vis absorption of **7a** in CH_2Cl_2 (10^{-5} M solution); (b) UV-Vis absorption of **7a** in absorption in TE + 1% DMSO (10^{-5} M solution). **Supporting Fig. S23:** (a) Fluorescence emission of **7a** in CH_2Cl_2 (10^{-5} M solution, $\lambda_{ex} = 550$); (b) Fluorescence emission of **7a** in absorption in TE + 1% DMSO (10^{-5} M solution, $\lambda_{ex} = 510$). **Supporting Fig. S24:** (a) Normalized fluorescence emission of **7a** in CH_2Cl_2 (10^{-5} M solution, $\lambda_{ex} = 550$); (b) Normalized fluorescence emission of **7a** in absorption in TE + 1% DMSO (10^{-5} M solution, $\lambda_{ex} = 510$). **Supporting Fig. S25:** (a) UV-Vis absorption of **7b** in CH_2Cl_2 (10^{-5} M solution); (b) UV-Vis absorption of **7b** in absorption in TE + 1% DMSO (10^{-5} M solution). **Supporting Fig. S26:** (a) Fluorescence emission of **7b** in CH_2Cl_2 (10^{-5} M solution, $\lambda_{ex} = 520$); (b) Fluorescence emission of **7b** in absorption in TE + 1% DMSO (10^{-5} M solution, $\lambda_{ex} = 490$). **Supporting Fig. S27:** (a) Normalized fluorescence emission of **7b** in CH_2Cl_2 (10^{-5} M solution, $\lambda_{ex} = 520$); (b) Normalized fluorescence emission of **7b** in absorption in TE + 1% DMSO (10^{-5} M solution, $\lambda_{ex} = 490$). **Supporting Fig. S28:** (a) UV-Vis absorption of **7c** in CH_2Cl_2 (10^{-5} M solution); (b) UV-Vis absorption of **7c** in absorption in TE + 1% DMSO (10^{-5} M solution). **Supporting Fig. S29:** (a) Fluorescence emission of **7c** in CH_2Cl_2 (10^{-5} M solution, $\lambda_{ex} = 560$); (b) Fluorescence emission of **7c** in absorption in TE + 1% DMSO (10^{-5} M solution, $\lambda_{ex} = 520$). **Supporting Fig. S30:** (a) Normalized fluorescence emission of **7c** in CH_2Cl_2 (10^{-5} M solution, $\lambda_{ex} = 560$); (b) Normalized fluorescence emission of **7c** in absorption in TE + 1% DMSO (10^{-5} M solution, $\lambda_{ex} = 520$). **Supporting Fig. S31:** (a) UV-Vis absorption of **7d** in CH_2Cl_2 (10^{-5} M solution); (b) UV-Vis absorption of **7d** in absorption in TE + 1% DMSO (10^{-5} M solution). **Supporting Fig. S32:** (a) Fluorescence emission of **7d** in CH_2Cl_2 (10^{-5} M solution, $\lambda_{ex} = 440$); (b) Fluorescence emission of **7d** in absorption in TE + 1% DMSO (10^{-5} M solution, $\lambda_{ex} = 380$). **Supporting Fig. S33:** (a) Normalized fluorescence emission of **7d** in CH_2Cl_2 (10^{-5} M solution, $\lambda_{ex} = 440$); (b) Normalized fluorescence emission of **7d** in absorption in TE + 1% DMSO (10^{-5} M solution, $\lambda_{ex} = 380$). **Supporting Fig. S34:** (a) UV-Vis absorption of **7e** in CH_2Cl_2 (10^{-5} M solution); (b) UV-Vis absorption of **7e** in absorption in TE + 1% DMSO (10^{-5} M solution). **Supporting Fig. S35:** (a) Fluorescence emission of **7e** in CH_2Cl_2 (10^{-5} M solution, $\lambda_{ex} = 520$); (b) Fluorescence emission of **7e** in absorption in TE + 1% DMSO (10^{-5} M solution, $\lambda_{ex} = 480$). **Supporting Fig. S36:** (a) Normalized fluorescence emission of **7e** in CH_2Cl_2 (10^{-5} M solution, $\lambda_{ex} = 520$); (b) Normalized fluorescence emission of **7e** in absorption in TE + 1% DMSO (10^{-5} M solution, $\lambda_{ex} = 480$). **Supporting Fig. S37:** (a) UV-Vis absorption of **7f** in CH_2Cl_2 (10^{-5} M solution); (b) UV-Vis absorption of **7f** in absorption in TE + 1% DMSO (10^{-5} M solution). **Supporting Fig. S38:** (a) Fluorescence emission of **7f** in CH_2Cl_2 (10^{-5} M solution, $\lambda_{ex} = 520$); (b) Fluorescence emission of **7f** in absorption in TE + 1% DMSO (10^{-5} M solution, $\lambda_{ex} = 480$). **Supporting Fig. S39:** (a) Normalized fluorescence emission of **7f** in CH_2Cl_2 (10^{-5} M solution, $\lambda_{ex} = 520$); (b) Normalized fluorescence emission of **7f** in absorption in

TE + 1% DMSO (10^{-5} M solution, $\lambda_{ex} = 480$). **Supporting Fig. S40:** (a) UV-Vis absorption of **5a-f** in CH_2Cl_2 (10^{-5} M solution); (b) UV-Vis absorption of **7a-f** in absorption in CH_2Cl_2 (10^{-5} M solution). **Supporting Fig. S41:** (a) UV-Vis absorption of **5a-f** in TE + 1% DMSO (10^{-5} M solution); (b) UV-Vis absorption of **7a-f** in absorption in TE + 1% DMSO (10^{-5} M solution). **Supporting Fig. S42:** (a) Fluorescence emission of **5a-f** in CH_2Cl_2 (10^{-5} M solution); (b) Fluorescence emission of **7a-f** in absorption in CH_2Cl_2 (10^{-5} M solution). **Supporting Fig. S43:** (a) Fluorescence emission of **5a-f** in TE + 1% DMSO (10^{-5} M solution); (b) Fluorescence emission of **7a-f** in absorption in TE + 1% DMSO (10^{-5} M solution). **Supporting Fig. S44:** Selectivity of cyanines **5a-f** (10^{-5} M solutions) versus different species of nucleic acids (0.5 mg/mL) in a TE buffer (solid bars) or in TE buffer containing 1% DMSO (dashed bars) at 20 °C. Experiments were performed in triplicate (error bar: mean standard deviation). Fluorescence intensity enhancement (I_{max}/I_0) were recorded at each dye's maximum emission, with excitation at the corresponding maximum absorption (see Table 1 in the main document). **Supporting Fig. S45:** Selectivity of cyanines **7a-f** (10^{-5} M solutions) versus different species of nucleic acids (0.5 mg/mL) in a TE buffer (solid bars) or in TE buffer containing 1% DMSO (dashed bars) at 20 °C. Experiments were performed in triplicate (error bar: mean standard deviation). Fluorescence intensity enhancement (I_{max}/I_0) were recorded at each dye's maximum emission, with excitation at the corresponding maximum absorption (see Table 1 in the main document). **Supporting Fig. S46:** ^{1}H NMR (500 MHz, CD_2Cl_2) of compound **5a** at different concentrations. (a) Aromatic signals (8.2-5.5 ppm); (b) Aliphatic signals (4.5-2.5 ppm). **Supporting Fig. S47:** ^{1}H NMR (500 MHz, CD_2Cl_2) of compound **5b** at different concentrations. (a) Aromatic signals (8.5-6.0 ppm); (b) Aliphatic signals (4.5-2.5 ppm). **Supporting Fig. S48:** ^{1}H NMR (500 MHz, CD_2Cl_2) of compound **5c** at different concentrations. (a) Aromatic signals (8.5-5.4 ppm); (b) Aliphatic signals (4.6-2.2 ppm). **Supporting Fig. S49:** ^{1}H NMR (500 MHz, CD_2Cl_2) of compound **5d** at different concentrations. (a) Aromatic signals (8.0-6.0 ppm); (b) Aliphatic signals (4.6-2.2 ppm). **Supporting Fig. S50:** ^{1}H NMR (500 MHz, CD_2Cl_2) of compound **5e** at different concentrations. (a) Aromatic signals (9.0-6.2 ppm); (b) Aliphatic signals (4.5-2.5 ppm). **Supporting Fig. S51:** ^{1}H NMR (500 MHz, CD_2Cl_2) of compound **5f** at different concentrations. (a) Aromatic signals (9.0-5.4 ppm); (b) Aliphatic signals (4.5-2.5 ppm). **Supporting Fig. S52:** UV–Vis absorption changes of pCp cyanine **5a** (10^{-5} M solution, TE buffer) induced by increasing tRNA concentrations (0.02-2 mg/mL). **Supporting Fig. S53:** UV–Vis absorption changes of pCp cyanine **5c** (10^{-5} M, TE buffer with 1% DMSO) induced by increasing tRNA concentrations (0.02-2 mg/mL). **Supporting Fig. S54:** Dissociation constant determination for racemic pCp-based cyanine **5a** (10^{-7} M solution in TE, $\lambda_{ex} = 550$ nm) and 10-loop (**D**). (a) Representative fluorescence titration; (b) Experiment 1; (c) Experiment 2; (d) Experiment 3. **Supporting Fig. S55:** Dissociation constant determination for racemic pCp-based cyanine **5c** (10^{-7} M solution in TE, $\lambda_{ex} = 560$ nm) and 10-loop (**D**). (a) Representative fluorescence titration; (b) Experiment 1; (c) Experiment 2; (d) Experiment 3. **Supporting Fig. S56:** Dissociation constant determination for racemic pCp-based cyanine **5a** (10^{-7} M solution in TE, $\lambda_{ex} = 550$ nm) and 8-loop (**C**). (a) Representative fluorescence titration; (b) Experiment 1; (c) Experiment 2; (d) Experiment 3. **Supporting Fig. S57:** Dissociation constant determination for pCp-based cyanine R_p-**5a** (10^{-7} M solution in TE, $\lambda_{ex} = 550$ nm) and 10-loop (**C**). (a) Representative fluorescence titration; (b) Experiment 1; (c) Experiment 2; (d) Experiment 3. **Supporting Fig. S58:** Dissociation constant determination for pCp-based cyanine S_p-**5a** (10^{-7} M solution in TE, $\lambda_{ex} = 550$ nm) and 10-loop (**C**). (a) Representative fluorescence titration; (b) Experiment 1; (c) Experiment 2; (d) Experiment 3. **Supporting Fig. S59:** Dissociation constant determination for racemic pCp-based cyanine **5c** (10^{-7} M solution in TE, $\lambda_{ex} = 560$ nm) and 8-loop (**C**). (a) Representative fluorescence titration; (b) Experiment 1; (c) Experiment 2; (d) Experiment 3. **Supporting Fig. S60:** Dissociation constant determination for racemic pCp-based cyanine **5c** (10^{-7} M solution in TE + 1% DMSO, $\lambda_{ex} = 560$ nm) and 8-loop (**C**). (a) Representative fluorescence titration; (b) Experiment 1; (c) Experiment 2; (d) Experiment 3. **Supporting Fig. S61:** Dissociation constant determination for racemic pCp-based cyanine **5a** (10^{-6} M solution in TE, $\lambda_{ex} = 550$ nm) and 6-loop (**B**). (a) Representative fluorescence titration; (b) Experiment 1; (c) Experiment 2; (d) Experiment 3. **Supporting Fig. S62:** Dissociation constant determination for racemic pCp-based cyanine **5c** (10^{-6} M solution in TE, $\lambda_{ex} = 560$ nm) and 6-loop (**B**). (a) Representative fluorescence titration; (b) Experiment 1; (c) Experiment 2; (d) Experiment 3. **Supporting Fig. S63:** Dissociation constant determination for racemic pCp-based cyanine **5a** (10^{-6} M solution in TE, $\lambda_{ex} = 550$ nm) and 4-loop (**A**). (a) Representative fluorescence titration; (b) Experiment 1; (c) Experiment 2; (d) Experiment 3. **Supporting Fig. S64:** Job plot for cyanine **5a** in the presence of 8-loop **C**. Data are presented as mean (error bar: standard deviation). **Supporting Fig. S65:** Crystal structure of compound **5a**. **Supporting Fig. S66**: Crystal packing of compound **5a**. **Supporting Fig. S67**: Crystal structure of compound **5b**. **Supporting Fig. S68**: Crystal packing of compound **5b**. **Supporting Fig. S69**: Crystal structure of compound **5c**. **Supporting Fig. S70**: Crystal packing of compound **5c**. **Supporting Fig. S71**: Crystal structure of compound **5e**. **Supporting Fig. S72**: Crystal packing of compound **5e**. **Supporting Fig. S73**: Crystal structure of compound **5f.** **Supporting Fig. S74**: Crystal paking of compound **5f**. **Supporting Table S1:** Detailed overview of fluorescence enhancements of cyanines **5a-f** (1 μM) versus different species of nucleic acids (0.5 mg/mL). **Supporting Table S2:** Detailed overview of fluorescence enhancements of cyanines **5a-f** (1 μM) versus different hairpin loops (1 μM). **Supporting Table S3:** Detailed overview of fluorescence enhancements of cyanines **7a-f** (1 μM) versus different species of nucleic acids (0.5 mg/mL). **Supporting Table S4:** Binding data from fluorescence titrations of racemic cyanine **5a** with 10-loop (**D**). **Supporting Table S5:** Binding data from fluorescence titrations of racemic cyanine **5c** with 10-loop (**D**). **Supporting Table S6:** Binding data from fluorescence titrations of racemic cyanine **5a** with 8-loop (**C**). **Supporting Table S7:** Binding data from fluorescence titrations of cyanine R_p-**5a** with 8-loop (**C**). **Supporting Table S8:** Binding data from fluorescence titrations of cyanine S_p-**5a** with 8-loop **C**. **Supporting Table S9:** Binding data from fluorescence titrations of racemic pCp-based cyanine **5c** with 8-loop **C**. **Supporting Table S10:** Binding data from fluorescence titrations of racemic pCp-based cyanine **5c** with 8-loop **C**. **Supporting Table S11:** Binding data from fluorescence titrations of racemic pCp-based cyanine **5a** with 6-loop **B**. **Supporting Table S12:** Binding data from fluorescence titrations of racemic pCp-based cyanine **5c** with 6-loop **B**. **Supporting Table S13:** Binding data from fluorescence titrations of racemic pCp-based cyanine **5a** with 4-loop **A**. **Supporting Table S14:** Spectroscopic measurements used to generate the job plot. The analyses were performed under the same conditions employed for the determination of the K_d values, using a total molar concentration of 5 x K_d and varying the **5a**/8-loop RNA ratios.; $\lambda_{ex} = 550$; $\lambda_{max} = 625$ nm). **Supporting Table S15:** Crystal data and structure refinement for racemic probe **5a** (fs469_0m). **Supporting Table S16:** Crystal data and structure refinement for racemic probe **5b** (rs98). **Supporting Table S17:** Crystal data and structure refinement for racemic probe **5c** (rs112_s2). **Supporting Table S18:** Crystal data and structure refinement for racemic probe **5e** (rs81). **Supporting Table S19:** Crystal data and structure refinement for racemic probe **5f** (rs120). **Supporting Table S20:** Summary of docking results for S_p-**5a** and R_p-**5a**.